A multimodal imaging and analysis pipeline for creating a cellular census of the human cerebral cortex

Irene Costantini *[1,2,3+]; Leah Morgan *[4]; Jiarui Yang *[6]; Yael Balbastre *[4,5]; Divya Varadarajan *[4,5]; Luca Pesce [1]; Marina Scardigli [1,7]; Giacomo Mazzamuto [1,3]; Vladislav Gavryusev [1,7]; Filippo Maria Castelli [1,7]; Matteo Roffilli [8]; Ludovico Silvestri [1,3,7]; Jessie Laffey [9]; Sophia Raia [9]; Merina Varghese [9]; Bridget Wicinski [9]; Shuaibin Chang [10]; Anderson Chen I-Chun [6]; Hui Wang [4,5]; Devani Cordero[4]; Matthew Vera [4]; Jackson Nolan[4]; Kim Nestor[4,5]; Jocelyn Mora [4,5]; Juan Eugenio Iglesias [4,5,11,12]; Erendira Garcia Pallares [4]; Kathryn Evancic[4,5] ; Jean Augustinack [4,5]; Morgan Fogarty [4]; Adrian V. Dalca [4,12]; Matthew Frosch [4]; Caroline Magnain [4,5]; Robert Frost [4,5]; Andre van der Kouwe [4,5]; Shih-Chi Chen [13]; David A. Boas [†6]; Francesco Saverio Pavone [†1,3,7]; Bruce Fischl [†4,5,12,14]; Patrick R. Hof [†9]

Affiliations

1. European Laboratory for Non-linear Spectroscopy (LENS), University of Florence, Sesto Fiorentino (FI), Italy
2. Department of Biology, University of Florence, Italy
3. National Institute of Optics (INO), National Research Council (CNR), Italy
4. Athinoula A. Martinos Center for Biomedical Imaging, Department of Radiology, Massachusetts General Hospital, Charlestown, MA, USA
5. Department of Radiology, Harvard Medical School, Boston, MA, USA
6. Boston University, Department of Biomedical Engineering, Boston, USA
7. Department of Physics and Astronomy, University of Florence, Sesto Fiorentino (FI), Italy
8. Bioretics srl, Cesena, Italy
9. Nash Family Department of Neuroscience and Friedman Brain Institute, Icahn School of Medicine at Mount Sinai, New York, NY, USA
10. Boston University, Department of Electrical and Computer Engineering, Boston, USA
11. Department of Medical Physics and Biomedical Engineering, University College London, London, UK
12. Computer Science and Artificial Intelligence Laboratory, Massachusetts Institute of Technology, Cambridge, MA, USA
13. The Chinese University of Hong Kong, Department of Mechanical Engineering, Hong Kong Special Administrative Region, China
14. HST, Massachusetts Institute of Technology, Cambridge, MA, USA

* These authors have contributed equally to this work and share first authorship
† These authors have supervised this work and share last authorship
+ Corrisponding author; email: costantini@lens.unifi.it

Abstract

Cells are not uniformly distributed in the human cerebral cortex. Rather, they are arranged in a regional and laminar fashion that span a range of scales. Here we demonstrate an innovative imaging and analysis pipeline to construct a reliable cell census across the human cerebral cortex. Magnetic resonance imaging (MRI) is used to establish a macroscopic reference coordinate system of laminar and cytoarchitectural boundaries. Cell counting is obtained with both traditional immunohistochemistry, to provide a stereological gold-standard, and with a custom-made inverted confocal light-sheet fluorescence microscope (LSFM) for 3D imaging at cellular resolution. Finally, mesoscale optical coherence tomography (OCT) enables the registration of the distorted histological cell typing obtained with LSFM to the MRI-based atlas coordinate system.

1 Introduction

The human brain is a complex organ organized across a range of spatial scales. To understand its properties and functionality, it is critical to produce a comprehensive characterization of the neuronal cell types that compose it and to visualize their distributions through the whole volume[1,2]. Although significant technological advances [3-7] have been made to obtain complete cell census in animal models such as mouse and marmoset monkey[8-16], no current imaging technology can directly visualize the defining microscopic features of the human brain without

significant distortion. Indeed, available cytoarchitectural parcellations of the human brain[17] are limited by unavoidable distortions introduced by slice-to-slice sectioning, clearing, staining and mounting steps involved in current histochemistry protocols. This processing results in artifacts that prevent accurate visualization of the tissue's morphomolecular properties such as individual cells across different regions or laminar and cytoarchitectural boundaries that form the natural coordinate system for a cell census of the human brain.

Important steps have been made towards building 3D models of the human brain with cellular resolution through the use of magnetic resonance imaging (MRI)[18-30], standard histology[31-38] and polarized light imaging (PLI[39]). For example, the Big Brain project[17] required 5 years and 1,000 person-hours to obtain a comprehensive dataset of one human brain with a nominal resolution of 20 µm. In parallel, data analysis and atlassing methods have been proposed to manage the the very large datasets generated during reconstructions and mapping of the volumes to standardized templates[6,40-42]. While these technologies represent remarkable advances, they still do not produce the undistorted 3D images of the cytoarchitecture of the human brain that are needed to build accurate models with nuclear and laminar resolution, a critical component of any cellular atlas.

Here, we present an innovative imaging and analysis pipeline that combines a number of imaging techniques to overcome the inherent limitations of each individual methodology. We propose to bridge microscopic volumetric histological imaging and macroscopic MRI using mesoscopic optical coherence tomography (OCT) to enable registration of the distorted histological volumes containing cell typing to an MRI-based atlas coordinate system. OCT is an optical technique that measures the backscattered light of the sample to provide high

resolution cross-sectional imaging and 3D reconstruction up to several hundred micrometers in depth in fixed *ex vivo* biological tissues, in a contact-free and non-invasive manner (no staining required)[43]. Serial sectioning OCT can be accurately registered to the whole -hemisphere MRI of the brain as imaging is performed prior to slicing and thus virtually minimal deformation is introduced. For 3D histological analysis with even higher sub-cellular resolution, confocal light-sheet fluorescence microscopy (LSFM)[44] is employed to image the large volumes of human brain tissue slabs obtained after OCT measurement. LSFM allows to obtain a fast optical sectioning of the sample by employing a specific configuration where the illumination axis is orthogonal to the acquisition axis[44-46]. LSFM is coupled with a dedicated tissue transformation technique to specifically label neuron subtypes and clear the tissue.

Finally, a stereological assessment is performed on the LSFM reconstructions to obtain a cell type-specific quantitative census of the neurons.

This multimodal imaging infrastructure was developed to bridge the resolution gap between macroscopic and microscopic techniques, resulting in a platform that integrates cellular anatomical information within a whole-brain reference space. The pipeline represents a large multi-institutional collaborative effort across the Massachusetts General Hospital, Boston University, the European Laboratory for Non-Linear Spectroscopy, and the Icahn School of Medicine at Mount Sinai.

2 Results

2.1 Imaging and Analysis Pipeline Overview

In this work, we generated a cell census of the human cerebral cortex by implementing a multimodal imaging and analysis pipeline on Broca's area (Brodmann's areas 44/45), blocked from whole human hemispheres. The postmortem specimen included in this project was obtained from a subject who had no neurologic or psychiatric illnesses. **Figure 1** provides an overview of the imaging pipeline performed on the sample (left, from top to bottom) and the subsequent imaging and data analysis pipeline (left to right). The whole hemisphere is first imaged with MRI before Broca's area is blocked and imaged with serial sectioning OCT. 3D histological fluorescence imaging on the acquired slices is then performed with LSFM. In parallel, gold-standard stereology is performed on additional tissue samples. A stereological evaluation is performed digitally on the LSFM data with a laminar level of resolution. An atlas of the data is obtained through non-linear registration of the three modalities; LSFM to OCT and OCT to MRI. Cell counts and manually labeled features are also registered along with the volumes on which they were generated, thereby mapping the results of our analysis to a within-subject coordinate system. All the data collected are made available on the DANDI platform[47]. In the following sections, details are provided on each step of this pipeline.

2.2 Reference coordinate system establishment with MRI imaging

A reference coordinate system for the cellular atlas was established with *ex vivo* MRI of the whole hemisphere. Structural images with 150-µm isotropic resolution were acquired using a multi-flip angle, multi-echo fast low angle shot (FLASH) MRI sequence on a Siemens 7 T MRI scanner using a custom-built 31-channel head coil[21]. We performed diffusion imaging on a Siemens 3 T MRI scanner using a Siemens 32-channel head coil. The MRI data were processed to correct for geometric distortions due to B_0 field inhomogeneities[48-50], contrast variations due to B_1transmit field inhomogeneities and intensity bias due to B_1 receive coil sensitivity variations[51]. **Figure 2** illustrates the 150-µm isotropic root mean squared (RMS) image for a flip angle of 20° calculated across the four echo times on the sample presented in this paper. **Figure 2** also demonstrates the improvement in vessel and laminar contrast quality attained by performing various artifact correction steps. **Figure 2a** zooms into the Broca's area where a clear contrast between grey and white matter, and the transition from the infra- to supragranular layer of the cortex within the grey matter, is visible in these images. These laminar boundaries are critical for tabulating information about cell types and their distributions within the characteristic architectural infrastructure that defines the cortical sheet. **Figure 2b** shows a zoomed-in portion of the frontal lobe that is severely effected by B_0 and B_1 transmit distortions. The B_0 inhomogeneity blurred the vessels and cortex in the RMS image due to misalignment between their locations in the different echo images. B1 transmit field variation reduced the overall vessel contrast. Vessels are important anatomical landmarks used to aid cross-modality registration and since the distortion corrected images demonstrate improved vessel sharpness and contrast, they aid in providing accurate landmarks essential for registration. **Figures 2c and 2d** show axial and sagittal slices before and after intensity bias

correction. The bias-corrected images show improved laminar and white matter contrast. The artifact-corrected whole-hemisphere MRI data presented here thus provides a reliable laminar framework, improved quality of vessel landmarks, and a reference space to which downstream modalities can be registered.

2.3 OCT 3D reconstruction for tissue registration

The excised block (approximately 1.5x1.3x0.8 cm^3) was imaged with a home-built serial sectioning OCT system at 5-µm isotropic mesoscale resolution that reveals cortical layers and cytoarchitectural boundaries[43]. To enhance the penetration of light deep inside the sample for OCT, we exploited a clearing procedure, based on the organic solvent 2,2'-thiodiethanol (TDE), to reach an imaging depth of up to 500 µm[52]. Sectioning the 500 µm-thick slices was performed using a custom-built vibratome that is capable of slicing sections up to 6 cm-wide[53]. By capturing the intrinsic back-scattering properties of the tissue, OCT elucidated features such as vasculature and cortical layer structure to be used as registration landmarks (**Figure 3** and **Supplementary Movie1**). Additionally, as OCT imaging precedes sectioning, tissue deformations from sectioning were almost completely eliminated.

2.4 Molecular phenotyping reconstruction with LSFM

Fluorescence imaging of the 16 slices was obtained using a custom-built dual-view inverted confocal LSFM with a voxel-size resolution of 0.55 x 0.55 x 3.3 $µm^3$ that results in a 3.3 $µm^3$ isotropic resolution after post-processing (**Figure 4a**)[54]. Molecular specificity was achieved by combining LSFM with an advanced tissue transformation protocol called SHORT[55]. The protocol

rendered the sample completely transparent to light by refractive index matching (**Figure 4b**) and allowed homogeneous co-labeling of large 3D volumes with different markers (**Figure 4c** and **Supplementary Figure 1**). To perform the cell census in the area 44/45, we used immunofluorescence to label specific neuronal populations. The use of neurochemical markers allows for the definition of region-specific staining patterns, and generally results in a high definition of cortical areas that complement traditional Nissl and myelin preparations. In this context, calcium-binding proteins have been shown to be reliable cellular markers for cytoarchitectural studies of the primate neocortex, in which they are present principally in distinct populations of inhibitory neurons that exhibit recognizable patterns of regional and laminar specialization[35,56-64]. We used an anti-neuronal nuclear antigen (NeuN) antibody to stain all neurons and an anti-calretinin (CR) antibody to identify a subpopulation of γ-aminobutyric acid-ergic (GABAergic) interneurons. To detect all cell nuclei we used an exogenous dye (propidium iodide, PI) obtaining a three-color costaining in the same tissue (**Figure 4d and Supplementary Movie 2**). Vessels were identified from autofluorescence signals generated by retained blood.

2.5 Stereological validation of 3D reconstruction

While LSFM enables the investigation of brain structures from the subcellular to the mesoscale, by recording different distributions of neuronal populations in large, cleared, specifically immunolabeled tissues with micrometric resolution and reasonably efficient acquisition times, no quantitative gold-standard validations of such population-level imaging data acquisitions currently exist. Hence we performed stereological gold-standard assessments on LSFM

reconstructions of identified neuronal populations using an Optical Fractionator probe[65,66] adapted to cleared materials (**Figure 5** and **Supplementary Figure 2**). We recorded on average 22,400 CR^+ neurons in layer 3 across the slabs, 85,500 $NeuN^+$ neurons in layer 3 and 62,700 $NeuN^+$ in layer 5, with corresponding densities of 2787, 8120, and 6168 neurons/mm^3, respectively (**Supplementary Table 1**).

These LSFM data were validated against stereologic estimates from separate specimens prepared using traditional protocols and analyzed under brightfield conditions (see supplementary materials). This provides the ability to compare manual estimates to automatic segmentations obtained from the same LSFM datasets, and ultimately to develop an integrated and unbiased quantitative database of identified cellular populations in the human neocortex. This parallel validation approach, performed on separate specimens prepared in thinner materials (50 µm-thick microtome sections of the entire area 44/45) and immunostained in series for each marker of interest, provides layer-specific estimates of cellular features, such as total numbers, local densities, somatic volumes, and spatial distribution of various neuronal populations identified by specific markers including cytoskeletal proteins, calcium-binding proteins, and neuropeptides, as well as generic cellular markers such as NeuN and the Nissl stain. These evaluations serve as a gold-standard for the project. Total neuronal number estimates based on Nissl-stained series of sections from the entire Broca's area yielded values averaging 35 million neurons in layer 3 and 22 million in layer 5, which is consistent with data obtained independently from prefrontal and temporal regions[67-69]. Preliminary assessment of a subpopulation of large pyramidal neurons identified by non-phosphorylated neurofilament protein (NPNFP) shows that these neurons account for about 30% of total neurons in both

layers 3 and 5 of the Broca's area (**Supplementary figure 3d**), in agreement with previous characterizations of this subset of projection neurons[62,68]. Also, individual Nissl-stained pyramidal cell volumes averaged 2,600 μm^3 in layer 5 and 2,400 μm^3 in layer 3, the NPNFP-immunoreactive cells being the largest ones with perikaryal volumes up to 6,000 μm^3. These preliminary observations are in agreement with previous characterizations of this subset of projection neurons[62,68].

2.6 Multimodal registration for MRI-referenced cell census

A defining feature of this project is processing the same human brain sample through each of the imaging techniques and quantitative tools described above. This enables us to place the cellular anatomical information within a cortical coordinate system. Cross-modality registration of cytoarchitectural properties is complicated due to distortions introduced by histological imaging techniques. While registration is facilitated by leveraging the fact that OCT is performed on the tissue block before sectioning, slices imaged with LSFM show significant distortions when compared to the OCT data. Hence we have developed a non-linear registration method that uses the segmentation of common features visible across all imaging modalities, such as blood vessels, to overcome this challenge. Vessels that have a diameter larger than 150 µm were manually segmented in MRI data and in each LSFM slice, and the Frangi filter[70] was used to segment vessel-like structures in OCT data (**Supplementary figure 4**). The resulting labels were used in a composite objective function that optimizes intensity similarity and label overlap to drive registration between MRI and OCT on one hand, and LSFM and OCT on the other hand.

We also demonstrate instantiation of microscopic cellular and stereologic information from distorted LSFM histological images within the MRI volume with OCT data serving as a critical intermediary modality with mesoscopic resolution and minimal distortion (**Figure 6** and **Supplementary Movie 3 and 4**). To the best of our knowledge, this is the first time that stereological annotations performed at the microscopic scale are mapped back into the space of the intact brain.

All deformations are fully invertible and allow any one modality to be warped to the space of any other modality. In addition to vasculature, the boundary between the cortical infra- and supragranular layers was segmented in MRI data and in a subset of LSFM slices to measure registration accuracy. The resulting transforms were used to warp the MRI segments to each manually segmented LSFM section (**Figure 7**), where the 95th (559 $\pm$ 200 µm) and 75th (310 $\pm$ 96 µm) percentiles of the minimum distance from the LSFM boundary to the MRI boundary were computed. It should be noted that these distances were computed in 2D sections and are therefore upper bounds on the 3D distances, and that 75% of boundary points have less than two voxels errors in the 150-µm isotropic MRI space.

Discussion

The pipeline presented here demonstrates the possibility of performing a cell census of the human brain, at micrometer resolution, by combining different techniques that overcome the inherent limitations associated with any single modality. To achieve this goal, we implemented new imaging and image processing approaches to correlate the four modalities involved: MRI, OCT, LSFM, and stereology. By first establishing a reference coordinate system for the cellular

atlas, through volumetric MRI, we greatly expand the utility of the cellular atlas and provide a basis for *in vivo* inferences with our analysis. Existing 3D models of the human brain with cellular resolution such as the Big Brain project[17] include sectioning distortions inherent to histology and do not permit through-plane tracing of features of interest across slices such as connecting axons, vasculature and laminar surfaces. However, the ability to build undistorted laminar models of the human cerebral cortex is a critical component of any cellular atlas. In the last decade, the combination of tissue clearing and high-throughput microscopy techniques, such as LSFM, have paved the way for the investigation of brain anatomy in 3D[71,72] with subcellular resolution. However, clearing methods and physical sectioning of the human brain sample introduce tissue distortions that complicate the coregistration between MRI reference data and fluorescence reconstructions. Attempts to perform MRI on cleared samples showed a contrast loss that prevents visualization of tissue microstructure[73], suggesting that MRI should be performed before tissue clearing. To facilitate the alignment between MRI and LSFM reconstruction, we decided to use OCT as an intermediate method with cellular resolution to enable registration of the distorted fluorescence images of cleared volumes to the MRI-based atlas coordinate system. We demonstrated for the first time accurate alignment of OCT and whole-hemisphere MRI of the brain at the vasculature level. As OCT data is acquired before slicing, it provides a critical, minimally distorted, intermediate reference between the MRI and LSFM.

Another important aspect of our pipeline is the choice of using immunofluorescence for specific identification of cellular markers both for LSFM imaging and stereological analysis. The precise immunoreactivity in neurons for neurochemical markers allows the definition of region-specific

staining patterns, and generally results in a better definition of the cortical areas compared to Nissl or myelin preparations. In this context, markers like neurofilament proteins and calcium-binding proteins are reliable cellular markers for the mammalian neocortex that identify distinct neuronal populations exhibiting recognizable patterns of regional and laminar specialization[35,56-58,60-64,74]. For example, NPNFP is present within a relatively small subset of large pyramidal neurons in layers 3, 5, and 6 that display a highly specific regional distribution[62,74-77]. Similarly, calcium-binding proteins and many neuropeptides are expressed in morphologically non-overlapping subgroups of GABAergic interneurons that are further classified by their electrophysiologic properties and local connectivity[78,79]. Interestingly, while these markers define generic classes of neurons, they also identify neuronal groups known to be differentially affected in many neuropsychiatric conditions. For example, NPNFP-enriched neurons are particularly affected in the course of Alzheimer's disease while GABAergic interneurons are spared[68,80], whereas in other conditions such as schizophrenia or autism spectrum disorder the same neurons present different vulnerability profiles[81-84].

Furthermore, this approach can be integrated with myeloarchitecture data and cerebral microvasculature distribution to enable the determination of patterns of molecular cytoarchitecture and connectivity on multiple scales, from single layers to columnar domains of cortex within a cortical region identified based on specific cytoarchitectural characteristics. To this end, we integrated analytical neurostereology techniques with layer-specific resolution within the pipeline[65,66]. These approaches are rigorous and validated, and have been extensively applied to the study of the human brain[68,69,85-89]. The analysis of multiple fluorescence channels on the same counting frame location is also possible[68]. Such

morphometric parameters can be used together with a combinatorial expression profiling analysis of cell classes to provide a comprehensive morphomolecular characterization of the cortical cellular typology[90]. A fundamental aspect of stereologic approaches is the accurate delineation of the region of interest. For Broca's area, we established reliable cyto- and chemoarchitectural criteria based on published studies[89,91,92]. Finally, stereology also provides a gold-standard against which automated approaches, such as machine learning-based methods to quantify cell types, can be verified. A final aspect of the proposed pipeline is the big data management that was optimized to allow the combination of the different techniques. Indeed, special attention was devoted to the choice of the nomenclature, reference data type format, compression, and post-processing methods to achieve a standardized procedure for data storage and sharing, replicable upon multiple samples.

Several challenges remain to be addressed further to improve the current pipeline.

The 3D stereological analysis employed in this study to obtain a reliable counting of cells is highly time-consuming. To obtain the census of the neurons in the entire acquired volumes, the raw images will be automatically analyzed. In particular, we are exploring the possibility of employing a convolutional neural network for pixel classification, previously proposed to analyze two-photon fluorescence microscopy images[93] and automatic cell detection obtained on mouse brain reconstruction with LSFM[55,94,95]. The approaches will be used to count the different neuronal populations stained in the samples automatically, providing a comprehensive characterization of the whole imaged volume. Moreover, to expand the molecular phenotyping of the tissue, multi-round staining on cleared sample[55,90,96] will be implemented to characterize human brain cytoarchitecture in greater details. In this context, a

quantitative database of morphofunctional neuronal types in identified cortical regions represents a crucial normative resource for the study of cellular changes in brain disorders. The consideration of differential cortical vulnerability in brain diseases can also be used for targeting key cortical domains to carry out future analyses. Also, to speed up the alignment process between the different techniques, eliminating the need to use manual landmarks as performed in this study, microstructure-informed automatic non-linear registration tools are needed. In this regard, we will enhance this pipeline through optimizing an automated vascular segmentation approach[97]. The reference labels will serve as examples to train segmentation models that will be used on future samples, bypassing manual annotation towards the creation of a scalable human brain cellular atlas.

The successful realization of this novel acquisition and analysis pipeline ensures reliable replicability across laboratories, representing a substantial scientific step forward in terms of rigor and reproducibility. We believe that the application of our multimodal approach will provide a deeper understanding of the human brain architecture across resolution levels. Our imaging technology pipeline will ultimately enable the automated reconstruction of undistorted 3D microscopic models of not just a brain area, but of an entire human brain, permitting the assessment of intra- and inter-subject variability. In turn, this will allow investigations of the presence and spread of pathologic cellular alterations observed in neuropsychiatric illnesses in which selective vulnerability of different cell types occur in disease-specific distribution patterns.

Methods

Human Brain sample collection

The samples used in this project were obtained from control subjects who died of natural causes with no clinical diagnoses or neuropathology. The brain hemisphere imaged for this paper was from a 79 year-old male. A standard fixation protocol was used in which brain was fixed in 10% formalin for a minimum of 90 days. The sample was packed in a 2% buffered paraformaldehyde solution for MRI scanning. After OCT imaging, tissue slices were stored in phosphate-buffered saline. Human brain tissue samples were procured from the Department of Neuropathology at the Massachusetts General Hospital (MGH) Autopsy Service (Boston, USA). Written consent was obtained from healthy participants prior to death, following IRB-approved tissue collection protocols from Partners Institutional Biosafety Committee (PIBC, protocol 2003P001937).

MRI imaging

Ex vivo MRI is performed on the whole human hemisphere using multiple flip angles of a multi-echo fast low-angle shot (ME FLASH or MEF) sequence at 150-µm isotropic resolution, on a 7 T Siemens MR scanner. Specific scan parameters were: TR = 34 ms, TE = 5.65, 11.95, 18.25 and 24.55 ms, respectively, field of view (FOV) = 192 x 81.3 mm, and slice thickness = 150 µm. A novel acquisition and optimization framework was developed to enhance signal-to-noise ratio (SNR) and correct geometric and intensity distortions without additional high-resolution scans. In the presence of B0 inhomogeneity, the odd and even echoes of the MEF are distorted in opposite directions because they are acquired with opposite polarity readout gradients[49,98]. To

remove these distortions, we collected a 2D-encoded B0 fieldmap, which estimates the amount of inhomogeneity at every voxel and in turn gives us a measure of displacement at every voxel of the 150-µm isotropic MEF. We acquired a standard gradient echo fieldmap consisting of two gradient echoes with TR = 5 s, FOV = 192 x 144 mm, matrix size = 160 x 120, and slice thickness = 1.2 mm. Geometric distortions are then corrected using a group sparsity-based edge preserving intensity correction algorithm that uses the fieldmap and all the FLASH images jointly to perform the correction[48]. Additionally, B1+ variation was estimated by acquiring multiple single echo FLASH sequences with short TE (2.7 ms), long TR (5 s), flip angles varying from 20° to 340°, FOV = 192 x 156 mm, matrix = 96 x 78, and slice thickness = 2 mm. We fit the frequency of the sinusoid at each voxel to estimate the multiplicative bias in our flip angle measurements. The estimated flip angle bias map was then used to correct the flip angle value at each voxel location. We fit T1 tissue parameter using a dictionary look up procedure and the corrected flip angle map. We synthesized new FLASH MRI scans with the estimated T1 using the MRI physics forward model for FLASH MRI contrast to remove variations caused by spatially non-uniform B1+ field[49,50].

The whole hemisphere was imaged using a custom-built 31-channel phased array coil[21] whose intrinsic sensitivity profile can cause non-uniform intensity. The lack of a body coil with a uniform receive sensitivity profile on the 7 T scanner makes acquisition-based receive bias estimation non-applicable to our scenario. We use a model-based B1- bias correction method that jointly segments tissue type at each voxel and estimates the intensity bias using a likelihood-based cost function. The method assumes that the voxels classified under the same tissue class will have the same FLASH intensity value[51].

Serial sectioning OCT imaging

A custom-built polarization-sensitive OCT (PSOCT) system was used to acquire the volumetric data, however, only the intensity signal was analyzed as the polarization part was beyond the scope of this study. Therefore, we use the terminology of OCT instead of PSOCT in the results. The system was built based on a previously reported setup[99] with a schematic as shown in **Figure 3a**. Specifically, a swept light source (AxsunTech) was used in the OCT system which has an A-line rate of 100 kHz, a center wavelength of 1310 nm and a bandwidth of 135 nm. The axial resolution was estimated to be 5.6 µm in tissue (with a refractive index of 1.4). The sample arm consists of a pair of XY scanning mirrors, a 4× telescope, and a 4× air objective (Olympus, UPLFLN4x, NA 0.13) to obtain a lateral resolution of 6 µm. The interference fringe from the sample and the reference arms was collected by a balanced detector. The post-objective power was measured to be 3.7 mW, achieving a 95 dB SNR. For this study, we used a 3x3 mm^2 FOV with a 3-µm lateral step size and 10% overlap between tiles, with each tile takes about 16 s. For large human brain blocks, the dimension of the embedded samples are usually a few centimeters on each dimension, which is over ten times greater than that of the FOV of a single image tile. Therefore, the whole sample surface was divided into a grid of views and the images from all views were stitched together to form a full surface. Motorized xyz stages (x and y stages: LTS150, Thorlabs; z stage: MLJ150, Thorlabs) were incorporated to translate the samples under the OCT scanning head to all the imaging locations. The maximum travel distance for x, y and z stages was 150 mm, 150 mm and 50 mm with correspondent one-direction moving accuracy of 2 µm, 2 µm and 10 µm. A customized vibratome slicer was mounted adjacent to the OCT imaging head to cut off a superficial slice of the tissue block upon completion of the

scanning of the sample surface. A 2.5-in custom sapphire blade (DDK) was vibrated at 50 Hz and 1.2 mm peak-to-peak amplitude while slicing, with 0.1 mm/s stage feed rate. Custom software written in LabVIEW was used to control OCT imaging and vibratome slicing.

The data acquisition computer was a high-performance local computer with a four-core processor, 64 GB memory, a high-speed digitizer (ATS9350, Alazar), a GPU (RTX4000, NVIDIA) and a 10 GB/s high-speed Ethernet card. Using the k-clock from the light source, the signal was digitized in even-k space. The GPU fetched the spectral domain data and performed real-space reconstruction on the fly, which included dispersion compensation[100], Fourier transform for depth-profile creation and rough trimming in depth. The reconstructed data was then saved to a local storage server with 28 TB space through the 10 GB/s Ethernet. Compared with the 0.2 GB/s data acquisition rate, the Ethernet transfer rate was much faster and helped avoid any data loss. For high-speed post processing, data saved in local server was automatically uploaded to Boston University Shared Computing Cluster (SCC), a high-performance computing resource located at the site of Massachusetts Green High Performance Computing Center at Holyoke, Massachusetts. Upon completion of the experiment, a parallelized post-processing script was executed on SCC which included distortion correction, volume stitching and various features extraction. We utilized both ImageJ plug-ins[101,102] and customized functions to correct distortion that is introduced during OCT acquisition, such as shading effect and gird distortion. To stitch the OCT volume in 3D, we first stitched tiles in 2D using the average intensity projection. After the coordination for each tile is obtained, we linearly blended them in x and y and then stacked them in z. Once the OCT volume is reconstructed, various features, such as

vessels, axonal bundles and cortical laminar structure can be extracted using feature enhancement algorithms.

Tissue clearing and labelling for LSFM imaging

Brodmann's areas 44/45 brain slices were treated with SHORT[55] a modified version of the SWITCH/TDE tissue transformation protocol from Costantini et al.[93], that combines the SWITCH technique[90] with the TDE clearing method[103]. Briefly, each slice was incubated in a SWITCH-off solution, consisting of 50% phosphate- buffered saline (PBS) titrated to pH 3 using HCl, 25% 0.1 M HCl, 25% 0.1 M potassium hydrogen phthalate, and 4% glutaraldehyde. After 24 h, the solution was replaced with PBS pH 7.4 with 1% glutaraldehyde. Finally, the samples were incubated in the clearing solution for 2-4 days at 55 °C. The presence of lipofuscin in the cellular soma[104] and the free-aldehyde double-bounds introduce high autofluorescence signals[105]. To decrease such spurious and non-specific signals, the specimens were treated with hydrogen peroxide (30% v/v) for 1 h at room temperature (RT). After several washes in PBS, antigen retrieval was performed using pre-heat tris-EDTA buffer (10 mM Tris base (v/v), 1 mM EDTA solution (w/v), 0.05% Tween 20 (v/v), pH 9) for 10 min at 95 °C. To perform the multicolour staining, after 3 washing steps with deionized water (DI) and rebalancing in PBS for 1 h, the samples were incubated with primary antibodies against NeuN (Merck ABN91 chicken) and calretinin (CR); Proteintech 12278-1-AP rabbit) at 37 °C for 4 days in PBS + 0.1% Triton (PBST). Dilutions for the anti-NeuN and -CR antibodies were 1:100 and 1:200 respectively). Following several washes in PBST, the samples were incubated for four days with the secondary antibodies conjugated with different Alexa Fluor dyes (dilution of 1:200). The slices were rendered transparent by soaking the samples in increasing solutions of 20%, 40% and 68%

(vol/vol) of 2,2'-thiodiethanol in PBS, each added with propidium iodide (dilution of 1:100) for 1-2 days at RT with gentle shaking. Samples were mounted in a sandwich- like configuration between a 250 µm thin quartz coverslip (for refractive index matching at a refractive index of 1.46) and a standard glass sample holder, with a 500 µm-thick steel spacer in between[55]. Glycerol (91%) in distilled water was used outside the sandwich for the LSFM objectives immersion. This step permitted us to achieve high penetration depth and to avoid any optical aberration by matching the refractive index of the brain samples.

LSFM imaging

In our custom-made inverted light-sheet fluorescence microscope[54], two identical objectives were inclined at 90° from each other and were spaced such that their fields-of-view (FOV) are orthogonal and overlap in the center. They alternately play excitation and detection roles. The objectives were a pair of LaVision Biotec LVMI-Fluor 12x PLAN with 12x magnification, NA 0.53, WD 8.5-11 mm, spherically and chromatically corrected in the visible range, with a correction collar for refractive index matching with the immersion solution. They were inclined at 45° relative to the sample holder plane to allow for the largest possible lateral sample size while not interfering with its extension within the plane. These objectives were carefully chosen to maximize the optical resolution (1.1 µm lateral and 3.7 µm axial) and field of view (1.1×1.1 mm^2), while respecting the geometrical constraints and allowing immersion in any refractive index matching media. The microscope was equipped with four laser sources (Cobolt MLD 405 nm/100 mW, MLD 488 nm/60 mW, DPL 561 nm/100 mW, MLD 638 nm/180 mW), each emitting a Gaussian beam that had its width adjusted by a dedicated telescope, before combining all of them through a set of three dichroic mirrors. This combined beam was split by

a 50-50% beam splitter in two equal parts that were conveyed into the two identical excitation pathways of the light-sheet microscope. In each pathway the beam was modulated in intensity, timing and transmitted wavelength by an acousto-optical tunable filter (AOTF, AAOptoelectronic AOTFnC-400.650-TN) and then was scanned by a galvo mirror (Cambridge Technology 6220H), in order to realize the digitally scanned light sheet planar illumination[106,107]. A scanning lens (Edmund Optics #45-353, fL=100 mm, achromat), placed after the galvo mirror, converted the angular deflection into a lateral displacement of the incident light. The beam was then directed by the excitation tube lens (Edmund Optics #45-179, fL=200 mm, achromat) to the objective's pupil, through which it sequentially illuminated neighboring lines within a single plane of the sample. Each objective was held on a motorized stage (PI L-509.14AD00) to adjust its focal plane position. The sample was held in a custom quartz sample holder inserted into a plastic tray filled with refractive index matching medium. The sample was positioned using a 3-axes motorized stage system (two PI M-531.DDG and a PI L-310.2ASD for a motion range within 30x30x2.5 cm^3 with submicrometric repeatability) and was imaged by translating it along the horizontal direction. The image velocity through the volume was 47 frames/s, corresponding to a volumetric rate of 0.5 cm^3/hour. The fluorescence emitted by the sample was collected by the other objective lens, then was separated from the reflected laser excitation light by a multi-band dichroic beam splitter (Semrock Di03-R405/488/561/635-t3-55x75), before being directed by the detection tube lens (Edmund Optics #45-179, fL=200 mm, achromat) on a sCMOS camera (Hamamatsu OrcaFlash4.0 v3). Each camera operated in confocal detection mode by having the rolling shutter sweep in synchrony with the galvo scan of the digital light sheet[95,108-112]. Five sets of band-pass filters were mounted in front of each camera on a motorized filter

wheel (Thorlabs FW102C) to image selectively the differently labeled cells or structures within the tissue sample.

The operation of the microscope hardware was controlled by a workstation running a custom multi-threaded software, developed in C++ using Qt with a flexible and modular architecture and composed now of approximately 9000 lines of code. Our software ensured hardware synchronization and triggering by using a National Instruments PCIe-6363 card and controlled the automatic image acquisition from the two sCMOS cameras in confocal detection mode, with a sustained data rate of 800 MB/s at 47 fps and storage on a 16 TB SSD RAID.

The acquisition procedure for any sample started from determining its edges. Each image stack was acquired by moving the sample along the x axis through the fixed FOVs of the two objectives, then the sample was shifted by 1 mm along the y axis and the next stack was acquired. This sequence continued until the whole volume had been acquired. Contiguous stacks had an overlap of 100 µm that allowed to fuse them in post-processing to form the whole volume. Appropriate metadata was saved jointly with the acquired stacks.

The two identical optical pathways of the LSFM alternately served as excitation and detection arms, with a time-delay of a half frame that was introduced between the two roles to avoid exposing the active rolling-shutter rows on the acquiring camera to stray light coming from the illumination beam on the same side. The two AOTF allowed to shutter each illumination pathway independently to avoid introducing stray light and, furthermore, enabled to select which laser wavelengths and intensities were impinging on the sample.

LSFM data management

To visualize the reconstruction of an entire slice, a post-processing pipeline was applied to the data. First, as the objectives acquire images of the moving sample at 45° relative to the slide plane, an affine transform was applied to compensate for the motion and the 45° rotation thus bringing the acquired volume back to the sample's coordinate system. The affine transform also performs a spatial down-sampling to 3.3-μm^3 isotropic resolution. Then a custom-made stitching software, ZetaStitcher (G. Mazzamuto, "ZetaStitcher: a software tool for high-resolution volumetric stitching" https://github.com/lens-biophotonics/ZetaStitcher), allowed us to fuse the contiguous stacks, using the overlapping regions, to obtain a representation of the whole sample. Only for visualization, an illumination intensity homogenization algorithm was applied to the stitched volume or to single slices to compensate variations in the laser beam power across the field of view and among stacks. For each fluorescence band, the observed intensity along the light propagation axis was averaged, attaining a smooth intensity profile. By dividing each image for this reference, illumination intensity artefacts occurring across the transversal sample extension were mitigated. To store and share the information, data was compressed using the JPEG2000 lossy approach that yields a 1:20 compression. The data analysis pipeline was written in Python. The 561 nm wavelength 3D reconstructions were used to visualize and segment the blood vessels to perform the alignment of the three modalities as described in the section below.

Stereology

Stereologic analysis was performed on each cleared slices of Broca's area, 500 µm-thick, imaged at a 3x3x3 µm pixels dimensions, and immunostained for NeuN and calretinin, using the

MBF Bioscience Stereo Investigator Cleared Tissue software (version 2020.1.1) with an Optical Fractionator design[65,66]. The counting frame size was 150 x 150 µm, the grid size was 800 x 800 µm, and the disector height was 15 µm for all sections of tissue examined generating >600 sampling sites. Layers 3 and 5 were outlined and their boundaries were used to estimate laminar surface areas and volume. There were 10 virtual 49.5 µm-thick sections for the tissue sample and layers 3 and 5 were contoured at the widest part of each sub-slab, with a 400% zoom. Markers were placed at the top of each sampled cell, as it came into focus within the depth of the disector.

Image registration

Intermodality deformations were modelled using a combination of affine and nonlinear transformations. The affine model was restricted to a similarity transform (i.e., combinations of translations, rotations and isotropic scaling) and encoded in the Lie algebra of the corresponding conformal Euclidean group[113]. Non-linear transformations were modelled by stationary velocity fields and exponentiated using a scaling and squaring algorithm[114], which ensures – under mild smoothness conditions – that the resulting transformations are invertible diffeomorphisms. The parameters of the deformations were optimized by minimizing a combination of losses on intensity images (normalized mutual information[115]) and manually segmented landmarks (soft Dice[116]). Stationary velocity fields were regularized with a combination of penalties on their bending and linear elastic energies[117]. When registering a whole volume (in this case, MRI) with a sub-block (e.g., OCT), the larger volume was always deformed to the space of the smaller block, where the objective function was computed. Because the transformation model is diffeomorphic, the resulting transforms could

nevertheless be inverted and used to warp the block back to the space of the larger volume. The same transforms were also used to warp stereology coordinates extracted from the MBF software. The registration model was implemented in PyTorch[118], leveraging automatic differentiation, and jointly optimized with Adam[119]. Parameters were progressively optimized in a coarse to fine fashion (rigid, then affine, then affine and nonlinear with a progressively finer grid), and the learning rate was divided by 10 when the objective function reached a plateau, until convergence. Specifically, for MRI to OCT registration, the OCT volume was downsampled to 100 µm, and normalized mutual information (NMI) was computed within patches of 150x150x150 voxels. The objective function combined NMI (weight 1), Soft Dice between grey matter segments (weight 1), Soft Dice between vessels segments (weight 0.1) and regularization (bending energy: 4, divergence: 1, shears: 4). For OCT to LSFM registration, the OCT volume was downsampled to 50/100/200 µm and the LSFM volumes were downsampled to 20/40/60 µm. The objective function was computed jointly at all resolutions and combined NMI (weight: 2), Soft Dice between vessels segments (weight: 0.1) and regularization (bending energy: 0.4, divergence: 0.1, shears: 0.4). The effect of different components of the SVF regularization was investigated in an ablation study. Dice scores between manually segmented vessels in the MRI and OCT volumes were computed in the initial position (*init*), after affine registration (*affine*) and after nonlinear registration with different composite types of regularization: the membrane energy (*membrane*) penalizes first derivatives, the bending energy (*bending*) penalizes second derivatives and the linear-elastic energy (*lame*) penalizes local shears and zooms. The best Dice score was obtained with a combination of bending and linear-elastic penalties.

567

FIGURES:

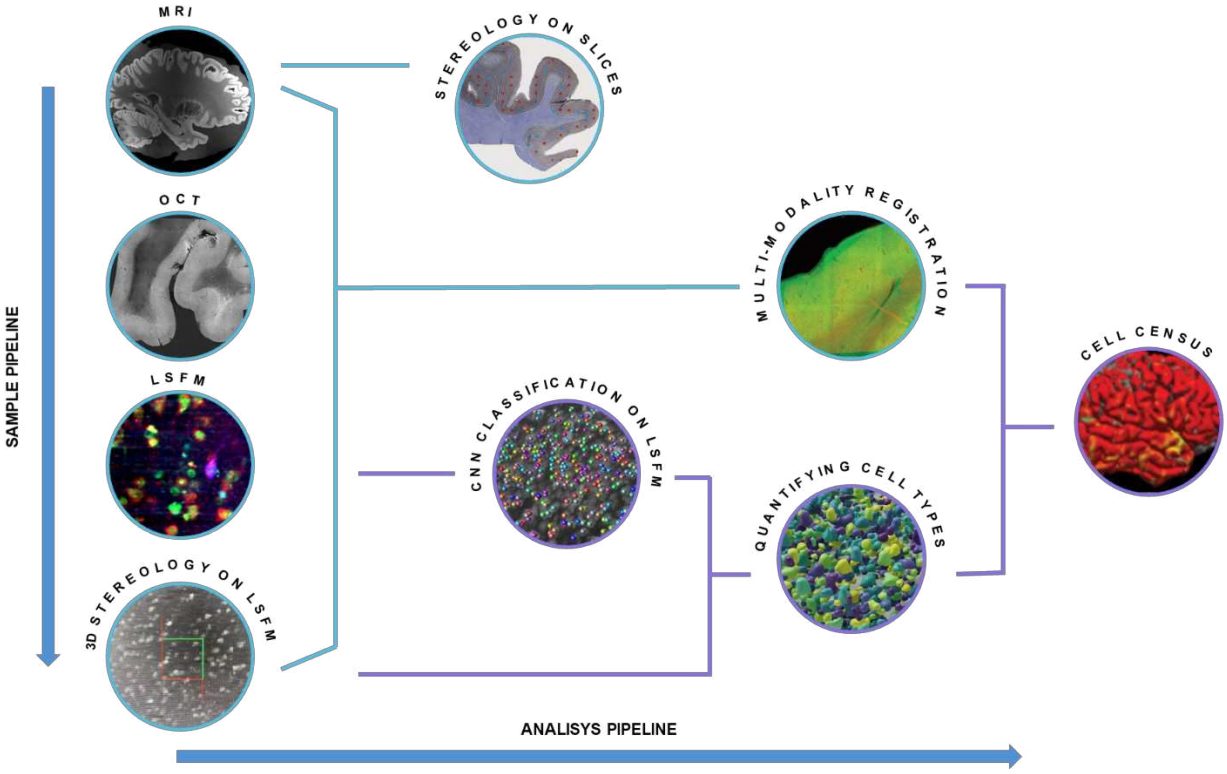

Figure 1: Imaging and analysis pipeline overview. From top to bottom sample pipeline: MRI, OCT, LSFM, and 3D stereology on LSFM images are performed on the same sample. Left to right analysis pipeline: thin-section stereology is performed on sections from separate specimens to obtain gold-standard counting; registration between MRI, OCT, LSFM and 3D sterology data is performed to align all the datasets back to the MRI coordinate system; cell counting with CNN classification on LSFM images will permit automatic counting of the stained neurons; the combination of 3D stereologic evaluation and CNN automatic counting will obtain a reliable quantification of cell types; multimodal registration between the images and the counting is needed to finally obtain the cell census of the neurons in a MRI-based atlas coordinate system. Schematic in cyan represents the steps presented in the current manuscript where a Broca's

580 Area block of tissue underwent to all the steps. Violet steps are future implementation of the

581 pipeline.

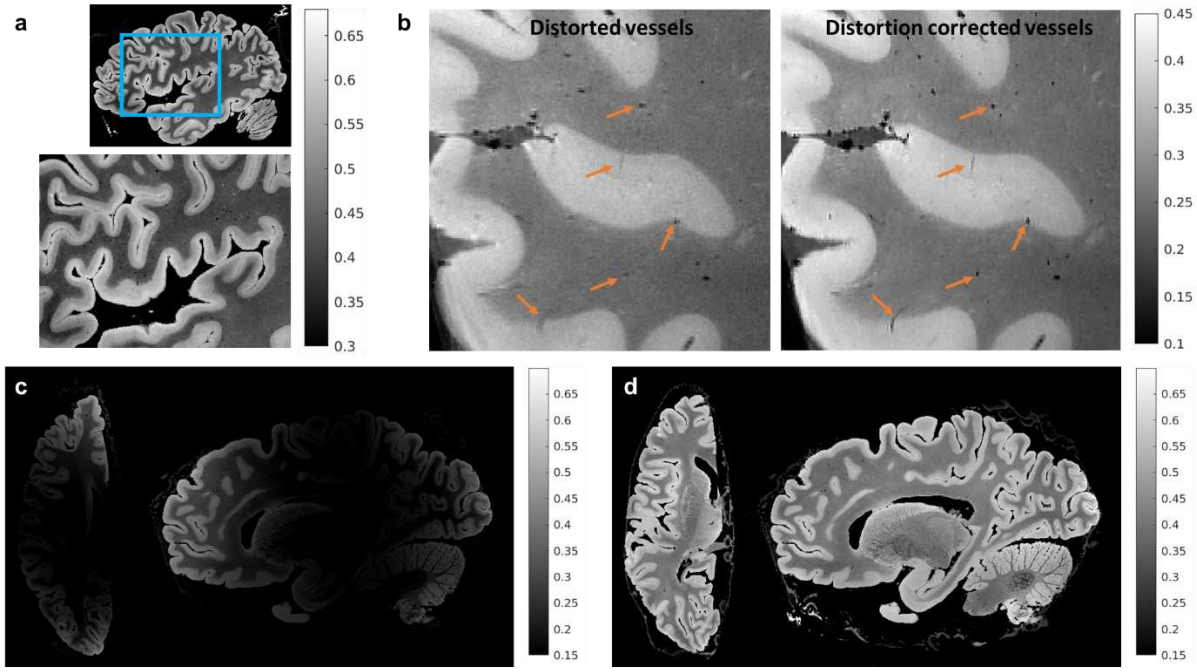

582

583 **Figure 2**: **MRI for global reference**. The figure shows results for 150 µm isotropic root mean

584 squared (RMS) FLASH MR images with RMS calculated across four echo times (TE= 5.65, 11.95,

585 18.25 and 24.55 ms) for a flip anlge of 20°. a) A sagittal section that is zoomed into the Broca's

586 area showing infra- and supra-granular gray matter contrast. b) A zoomed-in sagittal frontal

587 section of the same brain sample with vessels that are blurred and have reduced contrast. The

588 blurring is due to B0 field inhomogeneity while the reduced contrast is due to B1 transmit field

589 inhomogeneity. We also show vessels post-distortion correction that are well preserved and

590 have high contrast, demonstrating the effectiveness of the correction methods. c) and d) show

591 an axial and sagittal slice before and after B1 receive intensity bias correction. The intensities

592 are visibly more uniform after bias removal.

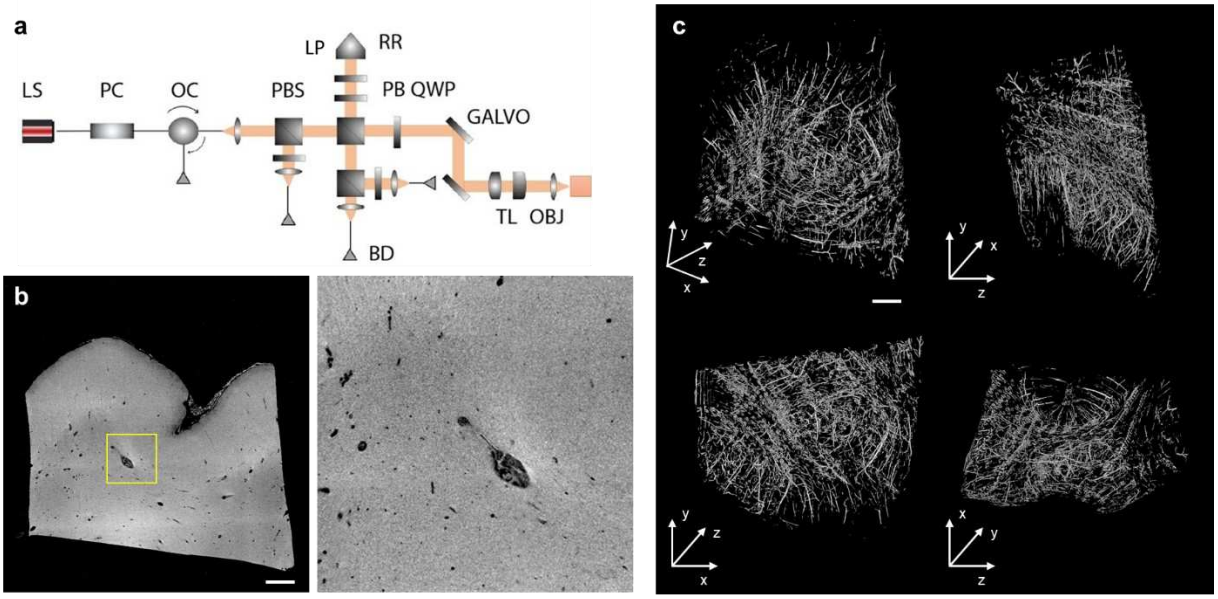

Figure 3: **OCT analysis.** a) Schematic of OCT. Annotations of components are LS: light source, PC: polarization controller, OC: optical circulator, PBS: polarizing beam splitter, PBS: polarization beamsplitter, RR: retroreflector, LP: linear polarizer,QWP: quarter wave plate, GALVO: galvo mirror, BD: balanced detector, TL: telescope, and OBJ: objective. b) An example XY slice of the OCT volume intensity (left) and zoom-in view of the highlighted window (right, dimension = 1.5 x 1.5 mm). Scale bar: 1 mm. c) 3D rendering and orthogonol views of the vessel segmentation of the OCT volume using the Frangi filtering method. Top left: 3D rendering view. Top right: YZ view. Bottom left: XY view. Bottom right: XZ view. Scale bar: 1 mm.

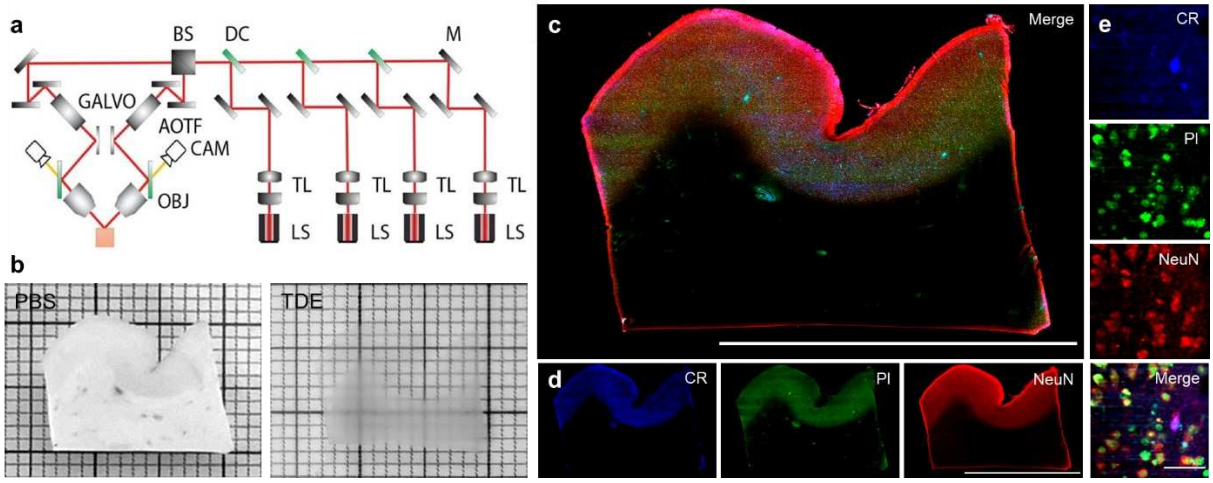

Figure 4: Multicolor imaging with LSFM. a) Schematic of LSFM apparatus. Annotations of components are LS: laser source, TL: telescope, M: mirror, DC: dichroic, BS: beam splitter, GALVO: galvo mirror, AOTF: acousto-optical tunable filters, CAM: camera, and OBJ: objective. b) A 500 µm-thick slice in PBS before (left) and after (right) TDE tissue clearing. c) A representative slice of a middle plane (≈200 µm depth) of a 500µm-thick slice stained with CR in blue (λ_{exc} =488), PI in green (λ_{exc} =561), and NeuN in red (λ_{exc} =638). Vessels are visible in the blue and green channels due to the presence of autofluorescence signals. d) Single channels of slice in c. Scale bars = 1 cm. e) High-resolution insets showing the different cellular markers used in the study: calretinin (CR), propidium iodide (PI), neuronal nuclear antigen (NeuN). Scale bar = 50 µm.

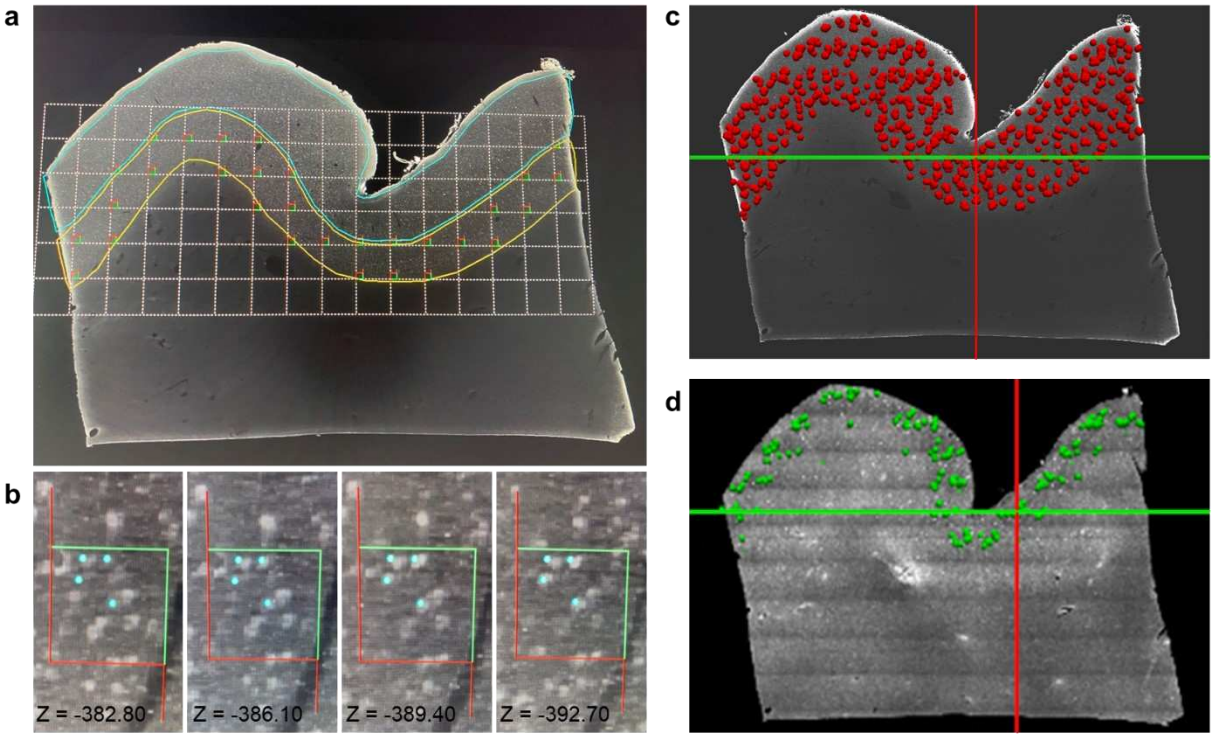

Figure 5: **Stereological evaluation on LSFM reconstructions.** a) A slab from the LSFM imaging dataset stained with the anti-NeuN antibody, displaying a systematic-random counting grid employed during stereologic analyses. The grid is placed over the infragranular layers (yellow outline) and optical disector frames are placed in all segments of the grid that are located within the region of interest. Panel b) shows different z-levels within a disector with blue markers indicating cells that have been sampled according to stereologic rules[38,39]. Panels c) and d) represent the registration of stereologic data onto the LSFM dataset for the entire slab. Each red dot in c) corresponds to $NeuN^+$ neurons sampled through the slab within an optical disector depth during stereologic analysis and used to generate an estimate of the total population number. The green dots in d) represent CR^+ neurons that were analyzed only in layers 2 and 3 as they are very sparse in the deep layers of the neocortex. Grid size on (a) = 800 μm, counting frame on (b) = 150 μm.

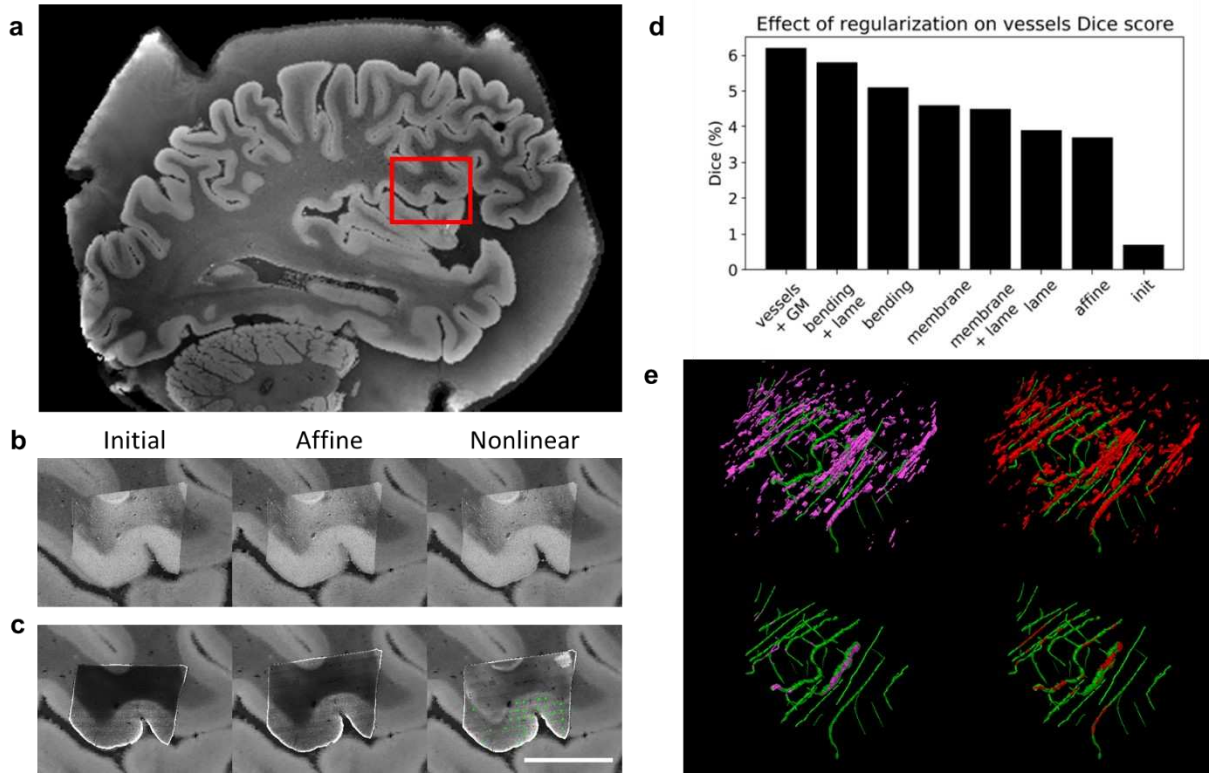

Figure 6: MRI, OCT, LSFM and stereology warped into a single coordinate space. Although the imaging data can be mapped into any space, we chose to display the alignment in OCT space, because it preserves the sectioning axis, allowing all modalities to be visible with minimal distortions. a) Panel showing the whole-hemisphere MRI image with a red box around area 44/45. b) Images showing the MRI deformed to OCT space after initialization, automated affine, and automated nonlinear registration. c) Images showing a slice of LSFM deformed to OCT space after initialization, automated affine, and automated nonlinear registration. The nonlinear registration panel further shows NeuN (green) and CR (red) counting coordinates obtained by stereology and warped to OCT space. d) Graph showing the effect of nonlinear regularization on vessels Dice score for MRI/OCT registration. *init*: initial alignment; *affine*: similitude with 7 degrees of freedom; *membrane*: penalty on first derivatives; *bending*: penalty on second derivatives; *lame*: penalty on zooms and shears, *vessels+GM*: bending+lame with the

addition of a vessel- and cortex-based objective function). Scale bar = 1 cm e) Images showing the vessels registration in MRI and OCT with and without a vessel-specific loss. The vessels manually segmented in the OCT volume (green) are shown alongside vessels manually segmented in the MRI volume and warped to the OCT volume using either a purely intensity-based objective function (pink) or a composite intensity- and vessel- based cost function (red).

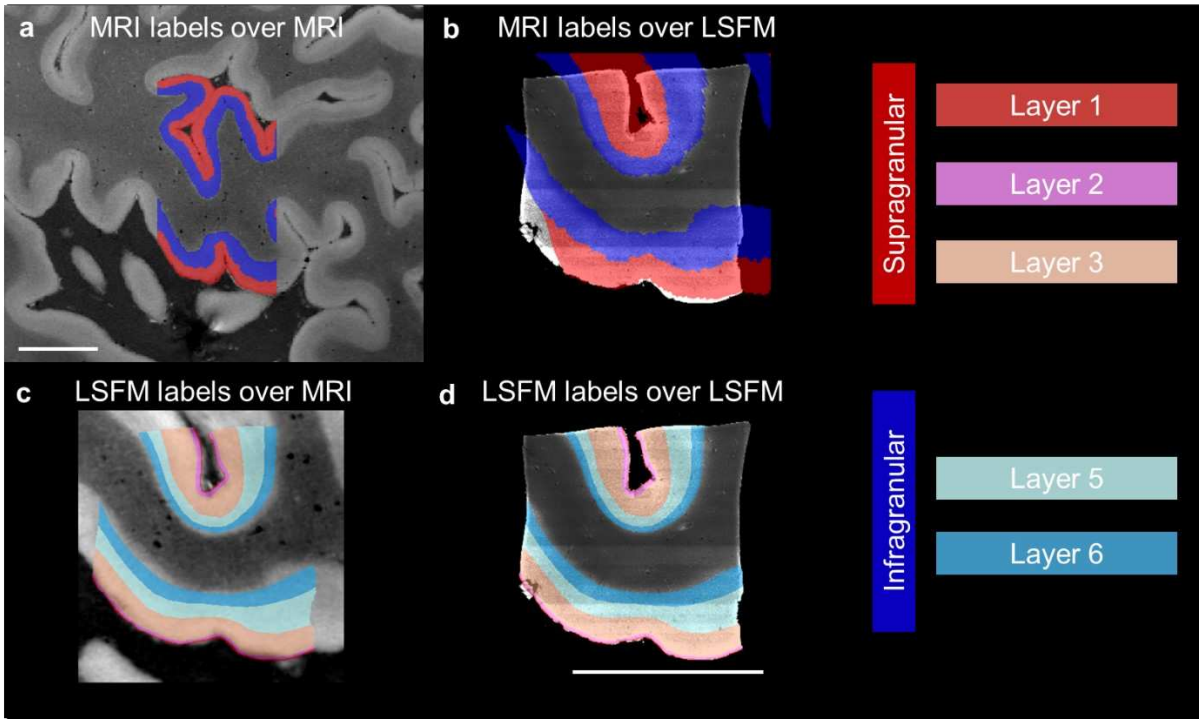

Figure 7: Overlap of Infragranular and supragranular laminar labels derived from MRI and LSFM after coregistration. a) MRI overlaid with the manually labeled infra- and supragranular layers. b) LSFM overlaid with the same MRI-derived labels after registration. c) MRI warped in LSFM space overlaid with LSFM-derived laminar labels. d) LSFM overlaid with manually labeled cortical layers. There is no internal granular layer 4 in Broca's area. Scale bars = 1cm.

Acknowledgements

We thank Jack Glaser and Julie McMullen (MBF Bioscience) for all their help during implementation of the Stereo Investigator Cleared Tissue software in our application. We express our gratitude to the donor involved in the body donation program of the Massachusetts General Hospital who made this study possible by generously donating his body to science. Support for this research was provided in part by the BRAIN Initiative Cell Census Network grant U01 MH117023, the National Institute for Biomedical Imaging and Bioengineering (P41 EB015896, R01 EB023281, R01 EB006758, R21E B018907, R01 EB019956, P41 EB030006, R00 EB023993), the National Institute on Aging (R56 AG064027, R01 AG064027, R01 AG008122, R01 AG016495), the National Institute of Mental Health (R01 MH123195, R01 MH121885, RF1 MH123195), the National Institute for Neurological Disorders and Stroke (R01 NS0525851, R21 NS072652, R01 NS070963, R01 NS083534, U01 NS086625, U24 NS10059103, R01 NS105820), Eunice Kennedy Shriver National Institute of Child Health and Human Development (R21HD106038), Chan-Zuckerberg Initiative DAF an advised fund of Silicon Valley Community Foundation grant number 2019-198101, and was made possible by the resources provided by Shared Instrumentation Grants S10 RR023401, S10 RR019307, and S10 RR023043. Additional support was provided by the NIH Blueprint for Neuroscience Research (U01 MH093765), part of the multi-institutional Human Connectome Project. This project has also received funding from European Union's Horizon 2020 research and innovation Framework Programme under grant agreement No. 654148 (Laserlab-Europe); European Union's Horizon 2020 Framework Programme for Research and Innovation under the Specific Grant Agreement No. 785907 (Human Brain Project SGA2), No. 945539 (Human Brain Project SGA3) and under

675 the Marie Skłodowska-Curie grant agreement No. 793849 (MesoBrainMicr); Italian Ministry for
676 Education in the framework of Euro-Bioimaging Italian Node (ESFRI research infrastructure);
677 "Fondazione CR Firenze" (private foundation), European Research Council (Starting Grant
678 677697, project BUNGEE-TOOLS), Alzheimer's Research UK (Interdisciplinary grant ARUK-
679 IRG2019A-003) and NIH R01 AG070988-01 and RF1 MH123195-01.
680 The content of this work is solely the responsibility of the authors and does not necessarily
681 represent the official views of the National Institutes of Health and other funding agencies.

682 Author Contributions

683 DV developed the B0 and B1 transmit distortion correction methods and the associated
684 imaging protocols to improve laminar and vessel contrast, optimized the scan protocol to
685 improve overall CNR and SNR of MRI and integrated intensity bias correction method into the
686 processing pipeline. AVDK developed the custom sequences used to acquire high resolution
687 structural MRI data, built the custom data-handling infrastructure and oversaw the
688 development of the MRI scan protocol with BF. DV, RF and LM contributed towards the
689 development of the MRI scan protocol, image acquisition, and analysis. YB contributed towards
690 the development of the multi-modal registration pipeline, building on original work done by JEI
691 and AD. MFr provided the human brain samples for this study. JA consulted on sample storage
692 and treatment for preservation throughout the imaging pipeline, including consulting on
693 histology protocols.
694 LM, DC, MVe, JN, KN, JM, EP, and KE performed the *ex vivo* imaging and analysis team and are
695 involved in image acquisition, data processing, and developing standards for segmenting

vasculature and the infra/supragranular boundary of the cortex. In MRI, OCT and LSFM data. DC, JN, KN, JM, EP, and KE performed manual labeling of these data. Labeling standards built on CM's original groundwork for segmenting features of interest for the purpose of registering MRI to OCT data. CM also consulted on OCT imaging and analysis for the BU team. LM oversaw the integration of the image and analysis pipeline and data publication for this project. This builds on MFo's original project oversight and management.

JY, SCha, HW, and IC developed and performed image acquisition and data processing of OCT measurement. JY, SCha, and SChe built the serial sectioning vibratome. JY coordinated the work on OCT sample preparation and transportation.

IC, LP, and MS developed and performed the clearing and staining protocol; VG, LS, and GM built the LSFM hardware and software apparatus, LP and VG performed light-sheet imaging. GM, FMC, VG, and MR contributed to image processing and data analysis. IC coordinated the work on sample preparation, image acquisition and data processing of LSFM measurement.

BW, MVa, SR and JL processed tissue for stereology and performed the stereologic analyses.

FSP, DAB, BF, and PRH conceived and supervised the study. BF helped design many of the algorithms used to analyze the data. IC, LM, JY, YB, DV, and PRH, wrote the paper with inputs from all authors.

Competing Interests Statement

BF has a financial interest in CorticoMetrics, a company whose medical pursuits focus on brain imaging and measurement technologies. BF's interests were reviewed and are managed by Massachusetts General Hospital and Partners HealthCare in accordance with their conflict of interest policies.

Data Availability

All the datasets acquired for this study are made available on the DANDI platform at the link:

https://gui.dandiarchive.org/#/dandiset/000026[47].

References

1 Kasthuri, N. & Lichtman, J. W. Neurocartography. *Neuropsychopharmacology* **35**, 342-343 (2010).

2 Venkataraju, K. U., Gornet, J., Murugaiyan, G., Wu, Z. & Osten, P. in *Neural Imaging and Sensing 2019.* 1086511 (International Society for Optics and Photonics).

3 Huang, S.-H. *et al.* Optical volumetric brain imaging: speed, depth, and resolution enhancement. *Journal of Physics D: Applied Physics* **54**, 323002 (2021).

4 Tyson, A. L. & Margrie, T. W. Mesoscale microscopy and image analysis tools for understanding the brain. *Progress in Biophysics and Molecular Biology* (2021).

5 Tward, D. *et al.* in *Multimodal Brain Image Analysis and Mathematical Foundations of Computational Anatomy.* (eds Dajiang Zhu *et al.*) 162-173 (Springer International Publishing).

6 Lee, B. C. *et al.* Multimodal cross-registration and quantification of metric distortions in marmoset whole brain histology using diffeomorphic mappings. *Journal of Comparative Neurology* **529**, 281-295, doi:https://doi.org/10.1002/cne.24946 (2021).

7 Lee, B. C., Tward, D. J., Mitra, P. P. & Miller, M. I. On variational solutions for whole brain serial-section histology using a Sobolev prior in the computational anatomy random orbit model. *PLoS Comput Biol* **14**, e1006610, doi:10.1371/journal.pcbi.1006610 (2018).

8 Bakken, T. E. *et al.* Comparative cellular analysis of motor cortex in human, marmoset and mouse. *Nature* **598**, 111-119 (2021).

9 Callaway, E. M. *et al.* A multimodal cell census and atlas of the mammalian primary motor cortex. *Nature* **598**, 86-102 (2021).

10 Muñoz-Castañeda, R. *et al.* Cellular anatomy of the mouse primary motor cortex. *Nature* **598**, 159-166 (2021).

11 Kim, Y. *et al.* Brain-wide Maps Reveal Stereotyped Cell-Type-Based Cortical Architecture and Subcortical Sexual Dimorphism. *Cell* **171**, 456-469.e422 (2017).

12 Lin, M. K. *et al.* A high-throughput neurohistological pipeline for brain-wide mesoscale connectivity mapping of the common marmoset. *Elife* **8** (2019).

13 Kasthuri, N. *et al.* Saturated Reconstruction of a Volume of Neocortex. *Cell* **162**, 648-661, doi:https://doi.org/10.1016/j.cell.2015.06.054 (2015).

14 Prasad, J. A. *et al.* A three-dimensional thalamocortical dataset for characterizing brain heterogeneity. *Sci Data* **7**, 358, doi:10.1038/s41597-020-00692-y (2020).

15 Network, B. I. C. C. A multimodal cell census and atlas of the mammalian primary motor cortex. *Nature* **598**, 86-102 (2021).

16 Ueda, H. R. *et al.* Whole-brain profiling of cells and circuits in mammals by tissue clearing and light-sheet microscopy. *Neuron* **106**, 369-387 (2020).

17 Amunts, K. *et al.* BigBrain: an ultrahigh-resolution 3D human brain model. *Science* **340**, 1472-1475 (2013).

18 Fischl, B. *et al.* Predicting the location of entorhinal cortex from MRI. *Neuroimage* **47**, 8-17 (2009).
19 Yushkevich, P. A. *et al.* A high-resolution computational atlas of the human hippocampus from postmortem magnetic resonance imaging at 9.4 T. *Neuroimage* **44**, 385-398 (2009).
20 Pfefferbaum, A., Sullivan, E. V., Adalsteinsson, E., Garrick, T. & Harper, C. Postmortem MR imaging of formalin-fixed human brain. *Neuroimage* **21**, 1585-1595 (2004).
21 Edlow, B. L. *et al.* 7 Tesla MRI of the ex vivo human brain at 100 micron resolution. *Sci Data* **6**, 244 (2019).
22 Roebroeck, A., Miller, K. L. & Aggarwal, M. Ex vivo diffusion MRI of the human brain: Technical challenges and recent advances. *NMR in Biomedicine* **32**, e3941 (2019).
23 Foxley, S. *et al.* Improving diffusion-weighted imaging of post-mortem human brains: SSFP at 7T. *NeuroImage* **102**, 579-589 (2014).
24 Miller, K. L., McNab, J. A., Jbabdi, S. & Douaud, G. Diffusion tractography of post-mortem human brains: Optimization and comparison of spin echo and steady-state free precession techniques. *NeuroImage* **59**, 2284-2297 (2012).
25 Miller, K. L. *et al.* Diffusion imaging of whole, post-mortem human brains on a clinical MRI scanner. *NeuroImage* **57**, 167-181 (2011).
26 Kolasinski, J. *et al.* A combined post-mortem magnetic resonance imaging and quantitative histological study of multiple sclerosis pathology. *Brain* **135**, 2938-2951 (2012).
27 Mollink, J. *et al.* Dentatorubrothalamic tract localization with postmortem MR diffusion tractography compared to histological 3D reconstruction. *Brain Structure and Function* **221**, 3487-3501 (2016).
28 Justine Beaujoin, C. D., Fabrice Poupon, Ilyess ZEMMOURA, Jean-François Mangin, Cyril Poupon. Post-mortem mapping of cortical layers using combined multicompartmental relaxometry and diffusometry at ultra-high field (7T and 11.7T). *ISMRM* (2018).
29 Justine Beaujoin, A. P., Raïssa Yebga Hot, Fabrice Poupon, & Jean-François Mangin, C. D., Cyril Poupon. CHENONCEAU: towards a novel mesoscopic (100/200µm) post-mortem human brain MRI atlas at 11.7T. *Organization for Human Brain Mapping* (2019).
30 Yann Leprince, B. S., Christophe Destrieux, Laurent Barantin, & Alexandre Vignaud, D. R., Cyril Poupon. Optimization of sample preparation for MRI of formaldehyde-fixed brains. *International Society for Magnetic Resonance in Medicine* (2015).
31 Juergen K Mai, M. M., George Paxinos. Atlas of the Human Brain. *Academic Press, London.*, 456 (2015).
32 Malikovic, A. *et al.* Cytoarchitectonic analysis of the human extrastriate cortex in the region of V5/MT+: a probabilistic, stereotaxic map of area hOc5. *Cereb Cortex* **17**, 562-574 (2007).
33 Morosan, P. *et al.* Human primary auditory cortex: cytoarchitectonic subdivisions and mapping into a spatial reference system. *Neuroimage* **13**, 684-701 (2001).
34 Schleicher, A., Amunts, K., Geyer, S., Morosan, P. & Zilles, K. Observer-independent method for microstructural parcellation of cerebral cortex: A quantitative approach to cytoarchitectonics. *Neuroimage* **9**, 165-177 (1999).
35 Ding, S. L. *et al.* Comprehensive cellular-resolution atlas of the adult human brain. *J Comp Neurol* **524**, 3127-3481 (2016).
36 Iglesias, J. E. *et al.* A probabilistic atlas of the human thalamic nuclei combining ex vivo MRI and histology. *NeuroImage* **183**, 314-326 (2018).
37 Adler, D. H. *et al.* Characterizing the human hippocampus in aging and Alzheimer's disease using a computational atlas derived from ex vivo MRI and histology. *Proceedings of the National Academy of Sciences* **115**, 4252 (2018).

38 Yushkevich, P. A. *et al.* Quantitative comparison of 21 protocols for labeling hippocampal subfields and parahippocampal subregions in in vivo MRI: Towards a harmonized segmentation protocol. *NeuroImage* **111**, 526-541 (2015).
39 Larsen, L., Griffin, L. D., Grassel, D., Witte, O. W. & Axer, H. Polarized light imaging of white matter architecture. *Microsc Res Tech* **70**, 851-863 (2007).
40 Banerjee, S. *et al.* Semantic segmentation of microscopic neuroanatomical data by combining topological priors with encoder-decoder deep networks. *Nat Mach Intell* **2**, 585-594, doi:10.1038/s42256-020-0227-9 (2020).
41 Majka, P. *et al.* Open access resource for cellular-resolution analyses of corticocortical connectivity in the marmoset monkey. *Nat Commun* **11**, 1133 (2020).
42 Tward, D. J., Mitra, P. P. & Miller, M. I. ESTIMATING DIFFEOMORPHIC MAPPINGS BETWEEN TEMPLATES AND NOISY DATA: VARIANCE BOUNDS ON THE ESTIMATED CANONICAL VOLUME FORM. *Q Appl Math* **77**, 467-488 (2019).
43 De Boer, J. F., Hitzenberger, C. K. & Yasuno, Y. Polarization sensitive optical coherence tomography–a review. *Biomedical optics express* **8**, 1838-1873 (2017).
44 Ueda, H. R. *et al.* Whole-Brain Profiling of Cells and Circuits in Mammals by Tissue Clearing and Light-Sheet Microscopy. *Neuron* **106**, 369-387 (2020).
45 Osten, P. & Margrie, T. W. Mapping brain circuitry with a light microscope. *Nature Methods* **10**, 515-523 (2013).
46 Franceschini, A., Costantini, I., Pavone, F. S. & Silvestri, L. Dissecting Neuronal Activation on a Brain-Wide Scale With Immediate Early Genes. *Front Neurosci* **14**, 569517 (2020).
47 Mazzamuto, G. *et al.* https://dandiarchive.org/dandiset/000026/draft. *U01MH117023 (Version draft) [Data set] DANDI archive* (2021).
48 Varadarajan, D., Frost, R., van der Kouwe, A., Morgan, L., Diamond, B., Boyd, E., Fogarty, M., Stevens, A., Fischl, B., and Polimeni, J.R., . Edge-preserving B0 inhomogeneity distortion correction for high-resolution multi-echo ex vivo MRI at 7T. *International Society for Magnetic Resonance in Medicine*, 664 (2020).
49 Fischl, B. *et al.* Sequence-independent segmentation of magnetic resonance images. *NeuroImage* **23**, S69-S84 (2004).
50 Deoni, S. C. L., Peters, T. M. & Rutt, B. K. High-resolution T1 and T2 mapping of the brain in a clinically acceptable time with DESPOT1 and DESPOT2. *Magnetic Resonance in Medicine* **53**, 237-241 (2005).
51 Van Leemput, K., Maes F Fau - Vandermeulen, D., Vandermeulen D Fau - Suetens, P. & Suetens, P. Automated model-based bias field correction of MR images of the brain.
52 Yang, J. *et al.* Improving the characterization of ex vivo human brain optical properties using high numerical aperture optical coherence tomography by spatially constraining the confocal parameters. *Neurophotonics* **7**, 045005 (2020).
53 Ragan, T. *et al.* Serial two-photon tomography for automated ex vivo mouse brain imaging. *Nature methods* **9**, 255-258 (2012).
54 Pesce, L. *et al.* Fast volumetric mapping of human brain slices. *Proc.SPIE* **11360** (2020).
55 Pesce, L. *et al.* 3D molecular phenotyping of cleared human brain tissues with light-sheet fluorescence microscopy. *bioRxiv*, 2021.2007.2018.452829 (2021).
56 Hendry, S. H. *et al.* Two classes of cortical GABA neurons defined by differential calcium binding protein immunoreactivities. *Exp Brain Res* **76**, 467-472 (1989).
57 Blumcke, I., Hof, P. R., Morrison, J. H. & Celio, M. R. Distribution of parvalbumin immunoreactivity in the visual cortex of Old World monkeys and humans. *J Comp Neurol* **301**, 417-432 (1990).
58 Hof, P. R., Nimchinsky, E. A., Celio, M. R., Bouras, C. & Morrison, J. H. Calretinin-immunoreactive neocortical interneurons are unaffected in Alzheimer's disease. *Neurosci Lett* **152**, 145-148 (1993).

59 Hof, P. R. *et al.* Parvalbumin-immunoreactive neurons in the neocortex are resistant to degeneration in Alzheimer's disease. *J Neuropathol Exp Neurol* **50**, 451-462 (1991).
60 Hof, P. R. & Morrison, J. H. Neocortical neuronal subpopulations labeled by a monoclonal antibody to calbindin exhibit differential vulnerability in Alzheimer's disease. *Exp Neurol* **111**, 293-301 (1991).
61 Hof, P. R., Mufson, E. J. & Morrison, J. H. Human orbitofrontal cortex: cytoarchitecture and quantitative immunohistochemical parcellation. *J Comp Neurol* **359**, 48-68 (1995).
62 Hof, P. R. & Morrison, J. H. Neurofilament protein defines regional patterns of cortical organization in the macaque monkey visual system: a quantitative immunohistochemical analysis. *J Comp Neurol* **352**, 161-186 (1995).
63 Carmichael, S. T. & Price, J. L. Architectonic subdivision of the orbital and medial prefrontal cortex in the macaque monkey. *J Comp Neurol* **346**, 366-402 (1994).
64 del Rio, M. R. & DeFelipe, J. Colocalization of calbindin D-28k, calretinin, and GABA immunoreactivities in neurons of the human temporal cortex. *J Comp Neurol* **369**, 472-482 (1996).
65 Schmitz, C. & Hof, P. R. Design-based stereology in neuroscience. *Neuroscience* **130**, 813-831 (2005).
66 Slomianka, L. Basic quantitative morphological methods applied to the central nervous system. *J Comp Neurol* **529**, 694-756 (2021).
67 Blinkov, S. M. & Glezer, I. B. i. a. I. *The human brain in figures and tables; a quantitative handbook*. (Basic Books, 1968).
68 Bussiere, T. *et al.* Stereologic analysis of neurofibrillary tangle formation in prefrontal cortex area 9 in aging and Alzheimer's disease. *Neuroscience* **117**, 577-592 (2003).
69 van Kooten, I. A. *et al.* Neurons in the fusiform gyrus are fewer and smaller in autism. *Brain* **131**, 987-999 (2008).
70 Frangi, A. F., Niessen, W. J., Vincken, K. L. & Viergever, M. A. in *Medical Image Computing and Computer-Assisted Intervention — MICCAI'98.* (eds William M. Wells, Alan Colchester, & Scott Delp) 130-137 (Springer Berlin Heidelberg).
71 Ueda, H. R. *et al.* Tissue clearing and its applications in neuroscience. *Nat Rev Neurosci* **21**, 61-79 (2020).
72 Costantini, I., Cicchi, R., Silvestri, L., Vanzi, F. & Pavone, F. S. In-vivo and ex-vivo optical clearing methods for biological tissues: review. *Biomed Opt Express* **10**, 5251-5267 (2019).
73 Morawski, M. *et al.* Developing 3D microscopy with CLARITY on human brain tissue: Towards a tool for informing and validating MRI-based histology. *Neuroimage* **182**, 417-428 (2018).
74 Hof, P. R., Nimchinsky, E. A. & Morrison, J. H. Neurochemical phenotype of corticocortical connections in the macaque monkey: quantitative analysis of a subset of neurofilament protein-immunoreactive projection neurons in frontal, parietal, temporal, and cingulate cortices. *J Comp Neurol* **362**, 109-133 (1995).
75 Hof, P. R., Cox, K. & Morrison, J. H. Quantitative analysis of a vulnerable subset of pyramidal neurons in Alzheimer's disease: I. Superior frontal and inferior temporal cortex. *J Comp Neurol* **301**, 44-54 (1990).
76 Hof, P. R. & Morrison, J. H. Quantitative analysis of a vulnerable subset of pyramidal neurons in Alzheimer's disease: II. Primary and secondary visual cortex. *J Comp Neurol* **301**, 55-64 (1990).
77 Campbell, M. J. & Morrison, J. H. Monoclonal antibody to neurofilament protein (SMI-32) labels a subpopulation of pyramidal neurons in the human and monkey neocortex. *J Comp Neurol* **282**, 191-205 (1989).
78 DeFelipe, J. *et al.* New insights into the classification and nomenclature of cortical GABAergic interneurons. *Nature Reviews Neuroscience* **14**, 202-216 (2013).

79 Petilla Interneuron Nomenclature, G. *et al.* Petilla terminology: nomenclature of features of GABAergic interneurons of the cerebral cortex. *Nat Rev Neurosci* **9**, 557-568 (2008).
80 Bussiere, T. *et al.* Progressive degeneration of nonphosphorylated neurofilament protei enriched pyramidal neurons predicts cognitive impairment in Alzheimer's disease: Stereologic analysis of prefrontal cortex area 9. *Journal of Comparative Neurology* **463** (2003).
81 Varghese, M. *et al.* Autism spectrum disorder: neuropathology and animal models. *Acta Neuropathol* **134**, 537-566 (2017).
82 Glausier, J. R., Roberts, R. C. & Lewis, D. A. Ultrastructural analysis of parvalbumin synapses in human dorsolateral prefrontal cortex. *J Comp Neurol* **525**, 2075-2089 (2017).
83 Glausier, J. R., Fish, K. N. & Lewis, D. A. Altered parvalbumin basket cell inputs in the dorsolateral prefrontal cortex of schizophrenia subjects. *Mol Psychiatry* **19**, 30-36 (2014).
84 Lewis, D. A., Curley, A. A., Glausier, J. R. & Volk, D. W. Cortical parvalbumin interneurons and cognitive dysfunction in schizophrenia. *Trends Neurosci* **35**, 57-67 (2012).
85 Bussière, T. *et al.* Progressive degeneration of nonphosphorylated neurofilament protein-enriched pyramidal neurons predicts cognitive impairment in Alzheimer's disease: stereologic analysis of prefrontal cortex area 9.
86 Akram, A. *et al.* Stereologic estimates of total spinophilin-immunoreactive spine number in area 9 and the CA1 field: relationship with the progression of Alzheimer's disease. *Neurobiol Aging* **29**, 1296-1307 (2008).
87 Uppal, N. *et al.* Neuropathology of the posteroinferior occipitotemporal gyrus in children with autism. *Mol Autism* **5**, 17-17 (2014).
88 Uppal, N. *et al.* Neuropathology of the anterior midcingulate cortex in young children with autism. *J Neuropathol Exp Neurol* **73**, 891-902 (2014).
89 Jacot-Descombes, S. *et al.* Decreased pyramidal neuron size in Brodmann areas 44 and 45 in patients with autism. *Acta Neuropathol* **124**, 67-79 (2012).
90 Murray, E. *et al.* Simple, Scalable Proteomic Imaging for High-Dimensional Profiling of Intact Systems. *Cell* **163**, 1500-1514 (2015).
91 Sherwood, C. C., Broadfield, D. C., Holloway, R. L., Gannon, P. J. & Hof, P. R. Variability of Broca's area homologue in African great apes: implications for language evolution. *Anat Rec A Discov Mol Cell Evol Biol* **271**, 276-285 (2003).
92 Amunts, K. *et al.* Broca's region revisited: cytoarchitecture and intersubject variability. *J Comp Neurol* **412**, 319-341 (1999).
93 Costantini, I. *et al.* Large-scale, cell-resolution volumetric mapping allows layer-specific investigation of human brain cytoarchitecture. *Biomed Opt Express* **12**, 3684-3699 (2021).
94 Frasconi, P. *et al.* Large-scale automated identification of mouse brain cells in confocal light sheet microscopy images. *Bioinformatics* **30**, i587-593 (2014).
95 Silvestri, L. *et al.* Universal autofocus for quantitative volumetric microscopy of whole mouse brains. *Nature Methods* (2021).
96 Chung, K. *et al.* Structural and molecular interrogation of intact biological systems. *Nature* **497**, 332-337 (2013).
97 Di Giovanna, A. P. *et al.* Whole-Brain Vasculature Reconstruction at the Single Capillary Level. *Scientific reports* **8** (2018).
98 van der Kouwe, A. J. W., Benner, T., Salat, D. H. & Fischl, B. Brain morphometry with multiecho MPRAGE. *NeuroImage* **40**, 559-569 (2008).
99 Golde, J. *et al.* Detection of carious lesions utilizing depolarization imaging by polarization sensitive optical coherence tomography. *Journal of biomedical optics* **23**, 071203 (2018).

100 Wojtkowski, M. *et al.* Ultrahigh-resolution, high-speed, Fourier domain optical coherence tomography and methods for dispersion compensation. *Optics express* **12**, 2404-2422 (2004).
101 Sorzano, C. O. S., Thévenaz, P. & Unser, M. Elastic registration of biological images using vector-spline regularization. *IEEE Transactions on Biomedical Engineering* **52**, 652-663 (2005).
102 Arganda-Carreras, I. *et al.* Consistent and Elastic Registration of Histological Sections Using Vector-Spline Regularization. *Computer Vision Approaches to Medical Image Analysis*, 85-95 (2006).
103 Costantini, I. *et al.* A versatile clearing agent for multi-modal brain imaging. *Scientific reports* **5**, 9808 (2015).
104 Pesce, L. *et al.* Exploring the human cerebral cortex using confocal microscopy. *Progress in Biophysics and Molecular Biology* (2021).
105 Costantini, I. *et al.* Autofluorescence enhancement for label-free imaging of myelinated fibers in mammalian brains. *Scientific reports* **11**, 8038 (2021).
106 Keller Philipp, J., Schmidt Annette, D., Wittbrodt, J. & Stelzer Ernst, H. K. Reconstruction of Zebrafish Early Embryonic Development by Scanned Light Sheet Microscopy. *Science* **322**, 1065-1069 (2008).
107 Olarte, O. E., Andilla, J., Gualda, E. J. & Loza-Alvarez, P. Light-sheet microscopy: a tutorial. *Adv. Opt. Photon.* **10**, 111-179 (2018).
108 Baumgart, E. & Kubitscheck, U. Scanned light sheet microscopy with confocal slit detection. *Opt. Express* **20**, 21805-21814 (2012).
109 Silvestri, L., Bria, A., Sacconi, L., Iannello, G. & Pavone, F. S. Confocal light sheet microscopy: micron-scale neuroanatomy of the entire mouse brain. *Opt Express* **20**, 20582-20598 (2012).
110 Mullenbroich, M. C. *et al.* Comprehensive optical and data management infrastructure for high-throughput light-sheet microscopy of whole mouse brains. *Neurophotonics* **2**, 041404 (2015).
111 Gavryusev, V. *et al.* Dual-beam confocal light-sheet microscopy via flexible acousto-optic deflector. *Journal of biomedical optics* **24**, 1-6 (2019).
112 Ricci, P. *et al.* Fast multi-directional DSLM for confocal detection without striping artifacts. *Biomed Opt Express* **11**, 3111-3124 (2020).
113 Ashburner, J. & Ridgway, G. R. Symmetric diffeomorphic modeling of longitudinal structural MRI. *Front Neurosci* **6**, 197 (2012).
114 Arsigny, V., Commowick, O., Pennec, X. & Ayache, N. A log-Euclidean framework for statistics on diffeomorphisms. *Med Image Comput Comput Assist Interv* **9**, 924-931 (2006).
115 Studholme, C., Hill, D. L. G. & Hawkes, D. J. An overlap invariant entropy measure of 3D medical image alignment. *Pattern Recognition* **32**, 71-86 (1999).
116 Sudre, C. H., Li, W., Vercauteren, T., Ourselin, S. & Jorge Cardoso, M. Generalised Dice Overlap as a Deep Learning Loss Function for Highly Unbalanced Segmentations. *Deep Learning in Medical Image Analysis and Multimodal Learning for Clinical Decision Support*, 240-248 (2017).
117 Ashburner, J. A fast diffeomorphic image registration algorithm. *Neuroimage* **38**, 95-113 (2007).
118 Paszke, A. *et al. PyTorch: An Imperative Style, High-Performance Deep Learning Library*. (2019).
119 Kingma, D. P. & Ba, J. Adam: A Method for Stochastic Optimization. *Proceedings of the 3rd International Conference on Learning Representations (ICLR 2015)* (2014).